Tenth International Conference on Computational Fluid Dynamics (ICCFD10), Barcelona, Spain, July 9-13, 2018

ICCFD10-2018-0016

Dedicated to the Memory of Dr. Meng-Sing Liou (NASA Glenn Research Center: 1987-2017)

Extension of AUSM-type schemes: from single-phase gas dynamics to multi-phase cryogenic flows

Chongam Kim*,** and Hyunji Kim*
Corresponding author: chongam@snu.ac.kr

*Department of Mechanical and Aerospace Engineering, Seoul National University, Korea.
**Institute of Advanced Aerospace Technology, Seoul National University, Korea.

Abstract: Despite its simple formulation, the AUSM-type flux schemes exhibit robust and accurate treatment of both linear and non-linear waves in complex flow fields. This paper presents the progress of AUSM-type fluxes augmented with pressure-based weight functions introduced by the authors and colleagues. Starting from a robust and accurate numerical flux designed for single-phase gas dynamics (AUSMPW+), extensions to capture multi-phase flow physics with phase transition (AUSMPW+_N) have been carried out. The accuracy of the computed results by AUSMPW+_N for multi-phase flows is then further improved by introducing a simple phase interface sharpening procedure, which scales the volume fraction in a mass-conserving manner. Various all-speed compressible tests ranging from interactions between a shock and a phase interface, two- and three-dimensional interface-only problems to a cryogenic three-component flow with phase change are computed to demonstrate the effectiveness of the proposed method.

Keywords: AUSMPW+_N, Interface Sharpening, Multi-phase Flow, Cryogenic flow.

1 Introduction

Numerical studies on compressible multi-phase flows have been carried out in a wide range of disciplines for decades, but are still challenging to perform due to the physical complexity intrinsic to multi-phase flows. (Throughout the paper, the tern "multi-phase flow" refers to multi-species and/or multi-phase flow; accordingly, "phase interface" refers to either the interface between different species or the interface between different phases of a single species.) Numerical methods, originally developed for single-phase gas dynamics, struggle to deal with such complex phenomena: the creation and evolution of another discontinuity (phase interface) besides a shock. Even though there exists a large disparity in material properties in both shock and phase interface, the fundamental wave natures of these discontinuities differ. Therefore, a numerical method for compressible multi-phase flows should be able to

(i) treat the shock and phase interface in different manners,

(ii) overcome the stiffness arising from the largely disparate flow speeds, pressures, and material properties,

(iii) demonstrate the travel and deformation of the phase interface over a long period of time,

(iv) include the creation/demise of the phase interface due to phase changes.

This becomes much more complicated when more than two phases exist. Thus, we add the condition that the numerical method for multi-phase flows should be able to

(v) readily include an additional phase without incurring a significant increase in computational complexity.

Depending on the way phase interfaces are treated, there are two types of numerical methods for describing two-phase flows: sharp interface methods and diffuse interface methods. Although sharp interface methods, such as the front-tracking method [1], the level-set method [2], or the ghost fluid method [3], can continuously maintain the sharp representation of a phase interface, they cannot handle dynamically created interfaces. If the condition (iv) is essential for the problem of interest, a diffuse interface method is adopted. Diffuse interface methods consider a phase interface as a diffused zone, not a sharp discontinuity, and can apply the same numerical method or model for both pure fluid and interface mixture zones. A dynamically created interface by phase change is naturally handled. However, the major drawback of diffuse interface methods is that interfaces are gradually smeared due to numerical diffusion.

A homogeneous mixture model, a type of diffuse interface method, is established based on the assumption of mechanical and thermal equilibrium between different phases in a computational cell. Although the detailed non-equilibrium effects at the phase interface could be reflected with more sophisticated non-equilibrium models [4, 5, 6], the homogeneous mixture approach is still attractive in respect of its simplicity as follows:

- One set of mass, momentum, and energy conservation laws is computed for the mixture, rather than multiple sets of conservation laws for each component.
- Extension to flows with three or more phases or species is readily acquired.
- Securing conservative and hyperbolic properties facilitates the use of numerical methods developed for single-phase gas dynamics.

For the sake of condition (v), we use the homogeneous mixture model to compute various multi-phase flows. Within the framework of a homogeneous mixture model, a robust numerical flux function that satisfies conditions (i) and (ii) and a numerical technique to manage the interface smearing for condition (iii) are necessary to meet the conditions listed above.

First, a robust numerical flux is required for compressible two-phase flows. Since the proposition of the original advection upstream splitting method (AUSM) [7] for gas dynamics, AUSM-type numerical fluxes have gained much attention and popularity. Despite its simple basic formulation, the AUSM scheme secures the robust and accurate treatment of both linear and non-linear waves in complex flow fields. Preserving the main idea of AUSM-type flux splitting, a series of sequels have been developed to overcome some defects and/or to extend the range of applications [8, 9]. This work presents the progresses of AUSM-type fluxes augmented with pressure-based weight functions introduced by the authors and colleagues [10, 11, 12]. Starting from a robust and accurate numerical flux designed for single-phase gas dynamics, extensions to multi-phase flow have been carried out with emphasis on conditions (i) and (ii).

Second, the diffuse interface model can be augmented with an interface-sharpening procedure to achieve condition (iii). Contrary to a shock wave which contains a physical compressive mechanism, a phase interface does not possess any physical means with which to counter numerical diffusion. Several studies provide numerical maneuvers to restore or preserve the sharp interface in compressible flows: the interface compression [13], anti-diffusion [14], tangent of hyperbola for interface capturing (THINC) [15] methods, TVD limiters [16, 17], and a level-set approach [18]. The present work proposes a simple but accurate interface-sharpening procedure with mass conservation.

After the brief introduction on the governing equation in Section 2, the extension of AUSMP-type numerical fluxes is presented. In Section 4, we explain the interface-sharpening method with mass conservation for the homogeneous mixture model. The results of validation tests of the proposed methods are shown in Section 5 and followed by the conclusion.

2 Numerical Modeling

2.1 Governing Equations

The homogeneous mixture model is adopted to describe multi-phase flows. The governing equations for the homogeneous mixture flow are expressed as

$$\frac{\partial}{\partial t}\int_{\Omega}\vec{W}\mathrm{d}\Omega+\oint_{\partial\Omega}\left[\vec{F}-\vec{F}_{\mathrm{v}}\right]\mathrm{d}S=\int_{\Omega}\vec{S}\mathrm{d}\Omega. \tag{1}$$

The vector of conservative variables $\vec{W}$ and the convective flux vector $\vec{F}$ are respectively given by

$$\vec{W}=\left[\rho\quad\rho u\quad\rho v\quad\rho E\quad\rho y_{\mathrm{v}}\quad\rho y_{\mathrm{g}}\right]^{\mathrm{T}}, \tag{2}$$

$$\vec{F}=\left[\rho U\quad\rho uU+n_xp\quad\rho vU+n_yp\quad\rho HU\quad\rho y_vU\quad\rho y_gU\right]^{\mathrm{T}}. \tag{3}$$

Here, $\vec{S}$ is the source term vector, and $U(\equiv n_xu+n_yv)$ is the contravariant velocity component normal to the surface element $\mathrm{d}S$. The mass fractions satisfy the following constitutive relation:

$$y_l+y_v+y_g=1, \tag{4}$$

where the subscripts (l, v, g) signify the liquid, gas phase of the same fluid, and non-condensable gas of another fluid, respectively. As represented in Eqs. (1)-(3), the consideration of the third phase (non-condensable gas) is achieved by the insertion of one more continuity equation.

2.2 Equation of State (EOS)

The governing equations are closed with equation of state for each component phase. For air and liquid water, stiffened-gas model is used.

$$p=(\gamma_i-1)\rho_i\frac{C_{p,i}}{\gamma_i}T-\gamma_ip_{\infty,i}\quad(i=l,\ v,\ g). \tag{5}$$

For cryogenic fluids, all thermodynamic properties of both liquid and vapor phases are generated from the standard reference database 23 available from the National Institute of Standard and Technology (NIST) [19]. To access these thermodynamic properties efficiently, we use the spline-based table look-up method [20].

The mixture density is then defined by the Amagat's law with the densities of the constituent phases:

$$\frac{1}{\rho}=\frac{(1-y_v-y_g)}{\rho_l}+\frac{y_v}{\rho_v}+\frac{y_g}{\rho_g}. \tag{6}$$

The mixture enthalpy is calculated as

$$h=h_l\left(1-y_v-y_g\right)+h_vy_v+h_gy_g. \tag{7}$$

2.3 System Preconditioning

In order to handle flows spanning from subsonic to supersonic Mach numbers, the governing equations (Eq. (1)) are preconditioned using the preconditioning matrix $\mathbf{\Gamma}$ of Weiss and Smith [21] as follows:

$$\mathbf{\Gamma}\frac{\partial}{\partial\tau}\int_{\Omega}\vec{Q}\mathrm{d}\Omega+\oint_{\partial\Omega}\left[\left(\vec{F}-\vec{F}_{\mathrm{v}}\right)\cdot\vec{n}\right]\mathrm{d}S=\int_{\Omega}\vec{S}\mathrm{d}\Omega. \tag{8}$$

The time variable t has been changed to τ, which indicates that Eq. (8) should be applied to steady computations. Here, $\vec{Q}$ stands for the vector of primitive variables given by $\vec{Q}=\left[p\quad u\quad v\quad T\quad y_{\mathrm{v}}\quad y_{\mathrm{g}}\right]^{\mathrm{T}}$. If $1/\beta$ inside $\mathbf{\Gamma}$ becomes $\frac{\partial\rho}{\partial p}$, then $\mathbf{\Gamma}$ goes back to the Jacobian matrix $\frac{\partial\vec{W}}{\partial\vec{Q}}$, resulting in a non-preconditioned

system in the primitive form. The eigenvalues of the preconditioned system in Eq. (8) are then given by

$$\lambda\left(\mathbf{\Gamma^{-1}}\frac{\partial\vec{F}}{\partial\vec{Q}}\right)=U,U,U,U,U'-D,U'+D,\quad U'=\frac{1}{2}\left(1+\frac{c'^2}{c^2}\right)U,\quad D=\frac{1}{2}\sqrt{\left(1-\frac{c'^2}{c^2}\right)^2U^2+4c'^2}. \tag{9}$$

The relation between $1/\beta$ and the preconditioned speed of sound c' is

$$\frac{1}{\beta}=\frac{1}{c'^2}-\frac{\frac{\partial\rho}{\partial T}\left(1-\rho\frac{\partial h}{\partial p}\right)}{\rho\frac{\partial h}{\partial T}} \tag{10}$$

with

$$c'=\min\left(c,\max\left(\sqrt{u^2+v^2},V_{\text{co}}\right)\right). \tag{11}$$

In Eq. (11), V_{co} is a cut-off value that is typically used to prevent c' from becoming zero in the vicinity of stagnation region. The cut-off value is generally specified as $V_{\text{co}}=kV_\infty$. For supersonic flows, the preconditioned speed of sound becomes the local speed of sound c, meaning that the preconditioning is turned off.

For unsteady low-Mach number computations, the dual time-stepping method is employed. When a physical time step Δt is large, the preconditioned speed of sound for steady flows (Eq. (11)) still works, but it causes unsatisfactory convergence behavior for intermediate and small time steps. In order to overcome this, Venkateswaran and Merkle [22] proposed a preconditioning method that takes the effect of the Strouhal number into account through von Neumann stability analysis. The resulting preconditioned speed of sound for unsteady flows c'_{un} is then given by

$$c'_{\text{un}}=\min\left(c,\max\left(\sqrt{u^2+v^2},V_{\text{co}},V_{\text{un}}\right)\right). \tag{12}$$

The unsteady preconditioning parameter is defined as $V_{\text{un}}=\frac{L_{\text{ch}}}{\pi\Delta t}=\frac{L_{\text{ch}}}{\pi\Delta tV}\times V=\text{Str}\times V$, where L_{ch} is a characteristic length scale. Although V_{un} was derived for single-phase gas flows, it is applicable to multi-phase flows because multi-phase effects induced by the homogeneous mixture model simply change the magnitude of the speed of sound. For steady flows or low Strouhal number flows with a large time step Δt, V_{co} is larger than V_{un}; consequently, c'_{un} is the same as c' in Eq. (11). For an intermediate time step, V_{un} can be larger than local velocity ($V=\sqrt{u^2+v^2}$) and unsteady preconditioning takes effect. As the time step becomes smaller for high Strouhal number flows, V_{un} completely turns off the system preconditioning, thus reverting the preconditioned speed of sound c' to the original speed of sound c. This corresponds to a physical situation where acoustic wave propagates with respect to the original speed of sound. Thus, Eq. (12) may promise an optimal convergence for inner iterations at all flow speeds and for all values of time step size.

More details on the numerical modeling for homogeneous multi-phase flows are found in the literature [12, 23].

3 AUSMP-type Numerical Fluxes with Pressure-based Weighting

In an effort to combine the accuracy of flux difference splitting (FDS) and the robustness of flux vector splitting (FVS), the AUSM [7] and its improved successors were published. Despite their respective improvements, AUSM$^+$ [8] and AUSMDV [24] were not perfectly free from numerical oscillations or the carbuncle phenomenon. By examining the complementary characteristics of these two schemes, AUSM by pressure-based weight functions (AUSMPW) [25] eliminated undesirable pressure wiggles and overshoots. Based on this history, more advanced AUSMP-type flux schemes have been developed.

3.1 AUSMPW+

Starting from the AUSMPW scheme, AUSMPW+ was designed to improve the accuracy and computational efficiency. By the new definition of numerical speed of sound at a cell interface, the resolution of oblique

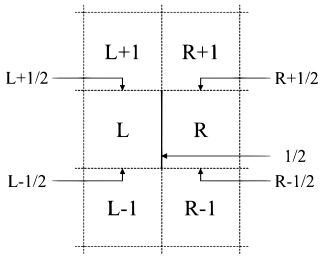

Figure 1: Interface of a two-dimensional cell

shock capturing was remarkably enhanced, and an unphysical expansion shock was completely excluded. The computational efficiency was also secured by simplifying the formulations.

For the Euler equations, the numerical flux of AUSMPW+ is written as

$$\vec{F} = \bar{\mathscr{M}}_L^+ c_{1/2} \vec{Q}_L^* + \bar{\mathscr{M}}_R^- c_{1/2} \vec{Q}_R^* + \vec{p}_{1/2}, \tag{13}$$

where $\vec{Q}^* = [\rho \quad \rho u \quad \rho v \quad \rho H]^{\mathrm{T}}$ and $\vec{p}_{1/2} = [0 \quad n_x p_s \quad n_y p_s \quad 0]^{\mathrm{T}}$. The pressure flux is

$$p_s = \mathscr{P}_L^+ p_L + \mathscr{P}_R^- p_R. \tag{14}$$

In Eq. (13), $\bar{\mathscr{M}}_{L,R}^{\pm}$ are defined as follows:

(i) for $m_{1/2} \geq 0$,

$$\bar{\mathscr{M}}_L^+ = \mathscr{M}_L^+ + \mathscr{M}_R^- [(1-w)(1+f_R) - f_L], \tag{15}$$

$$\bar{\mathscr{M}}_R^- = \mathscr{M}_R^- w(1+f_R), \tag{16}$$

(ii) for $m_{1/2} < 0$,

$$\bar{\mathscr{M}}_L^+ = \mathscr{M}_L^+ w(1+f_L), \tag{17}$$

$$\bar{\mathscr{M}}_R^- = \mathscr{M}_R^- + \mathscr{M}_L^+ [(1-w)(1+f_L) - f_R], \tag{18}$$

where $m_{1/2} = \mathscr{M}_L^+ + \mathscr{M}_R^-$. The Mach number and pressure splitting functions, $\mathscr{M}_{L,R}^{\pm}$ and $\mathscr{P}_{L,R}^{\pm}$, are obtained using the Mach number of each side $M_{L,R} = U_{L,R}/c_{1/2}$ as follows:

$$\mathscr{M}^{\pm} = \begin{cases} \pm\frac{1}{4}(M \pm 1)^2 & \text{for } |M| \leq 1, \\ \frac{1}{2}(M \pm |M|) & \text{for } |M| > 1, \end{cases} \tag{19}$$

$$\mathscr{P}^{\pm} = \begin{cases} \pm\frac{1}{4}(M \pm 1)^2 (2 \mp M) \pm \alpha M \left(M^2 - 1\right)^2 & \text{for } |M| \leq 1, \\ \frac{1}{2}(1 \pm \mathrm{sign}\,(M)) & \text{for } |M| > 1. \end{cases} \tag{20}$$

In order to prevent unwanted near-wall oscillations and overshoots behind a strong shock, the AUSMPW+ scheme introduced pressure-based weight functions f and ω:

$$f_{L,R} = \begin{cases} \left(\frac{p_{L,R}}{p_s} - 1\right) \min\left(1, \frac{\min(p_{L+1}, p_{R+1}, p_{L-1}, p_{R-1})}{\min(p_L, p_R)}\right)^2 & \text{for } p_s \neq 0 \\ 0 & \text{elsewhere} \end{cases}, \quad \omega = 1 - (\Pi_{1/2}^o)^3, \tag{21}$$

where

$$\Pi_{1/2}^o = \min\left(\frac{p_L}{p_R}, \frac{p_R}{p_L}\right). \tag{22}$$

The computational stencil for f which considers pressures in the transverse direction is shown in Fig. 1.

In AUSM-type fluxes, the definition of numerical speed of sound at a cell interface is critical to the resolution of a shock discontinuity. The AUSM$^+$ was able to capture the stationary normal shock exactly

with the common speed of sound at interface:

$$c_{1/2} = \min(\tilde{c}_L, \tilde{c}_R), \quad \tilde{c} = c^{*2}/\max(c^*, |U|), \tag{23}$$

where the critical speed of sound, c^*, is given by $\sqrt{2(\gamma-1)H/(\gamma+1)}$ for a calorically perfect gas. The AUSMPW+ scheme improved the shock-capturing property by defining a new interfacial speed of sound according to flow directions as:

$$c_{1/2} = \begin{cases} c_s^2/\max(c_s, |U_L|) & \text{for } (U_L + U_R) > 0 \\ c_s^2/\max(c_s, |U_R|) & \text{for } (U_L + U_R) < 0, \end{cases} \tag{24}$$

where the speed of sound normal to a cell interface, c_s, is given by $\sqrt{2(\gamma-1)H_{normal}/(\gamma+1)}$ for a calorically perfect gas. The AUSMPW+ with the new $c_{1/2}$ shows the exact capture of a stationary oblique shock and also eliminates the physically unaccepted expansion shocks. Detailed analysis and extensive validation results are found in Kim *et al.* [10].

3.2 AUSMPW+ for Gas-Liquid Two-phase Mixture Flows

The AUSMPW+ scheme which verifies its accuracy, efficiency, and robustness in gas dynamics were extended to gas-liquid two-phase mixture flows [11]. Above all, the advection variable vector in Eq. (13) was changed to $\vec{Q}^* = [\rho \quad \rho u \quad \rho v \quad \rho H \quad \rho y_v]^{\mathrm{T}}$ to include additional phase in two-phase mixture flows. The distinctive modifications in the two-phase AUSMPW+ are summarized below.

- **Numerical speed of sound at a cell interface**
  Since there is no Prandtl-like relation across a phase interface, the numerical speed of sound, $c_{1/2}$ in Eq. (24), should be modified to reflect the property of sound speed in a two-phase mixture. The homogeneous mixture model yields a lower sound speed in mixture than that of either phase; any interfacial speed of sound defined from some averaged mass fraction satisfies this property. For example, $c_{1/2}$ can be obtained from a Roe-type averaged enthalpy and mass fraction:

  $$c_{1/2} = c_{1/2}(p_{1/2}, \hat{h}, \hat{y_v}), \tag{25}$$

  where $p_{1/2} = 0.5(p_L + p_R)$.

- **Shock-discontinuity-sensing term (SDST) directly from the two-phase EOS**
  Even in subsonic two-phase flows, the pressure field can vary drastically due to the large density and high speed of sound in the liquid phase. Therefore, the original SDST of Eq. (22), which considers only the pressure ratio to detect a shock, grossly misinterpret the physically non-shock region as a shock region. A two-phase SDST was derived from the analysis based on the ideal gas law (for gas phase) and the stiffened-gas model (for liquid phase):

  $$\Pi_{1/2} = \min\left(\frac{\bar{p}_L}{\bar{p}_R}, \frac{\bar{p}_R}{\bar{p}_L}\right), \quad \bar{p}_{L,R} = 1/\left(\frac{\alpha_{v,1/2}}{p_{L,R}} + \frac{1-\alpha_{v,1/2}}{p_{L,R}+p_c}\right). \tag{26}$$

  In addition, following the M-AUSMPW+ [26] published after AUSMPW+, the pressure-based weight functions with the two-phase SDST are defined as

  $$f_{L,R} = \left(\frac{\bar{p}_{L,R}}{\bar{p}_s} - 1\right) \times (1-\omega), \quad \omega = \max(\omega_1, \omega_2), \tag{27}$$

  with

  $$\omega_1 = 1 - (\Pi_{1/2})^3, \quad \omega_2 = 1 - \left(\frac{\min(\bar{p}_{L+1}, \bar{p}_{R+1}, \bar{p}_{L-1}, \bar{p}_{R-1})}{\max(\bar{p}_{L+1}, \bar{p}_{R+1}, \bar{p}_{L-1}, \bar{p}_{R-1})}\right)^2.$$

- **Pressure-based weight function $f_{L,R}$ for large density ratio**
  The AUSMPW+ and its variants possess the pressure difference term in the mass flux, with the help of the pressure-based weight function as $\Delta f \propto \Delta p$. If the pressure difference coincides with a large-density-ratio phase interface, the mass flux induced by pressure difference becomes too large, which leads to numerical instability. To circumvent such instability, the function $f_{L,R}$ was modified by considering the densities on both sides:

$$f_{L,R} = \left(\frac{\bar{p}_{L,R}}{\bar{p}_s} - 1 \right) \times (1 - \omega) \times \frac{\min(\rho_L, \rho_R)}{\rho_{L/R}}, \tag{28}$$

  where

$$\rho_{L/R} = \begin{cases} \rho_L & \text{for } m_{1/2} \geq 0 \\ \rho_R & \text{for } m_{1/2} < 0 \end{cases}.$$

After the modifications, the two-phase AUSMPW+ was preconditioned for all-speed computations.

- **Scaling for low Mach number flows**
  The scaling technique by Edwards and Liou [27] was adopted. The Mach number and pressure splitting functions (Eqs. (19) and (20)) were evaluated using the following scaled Mach number:

$$M^*_{1/2} = \frac{1 + M^2_{r,1/2}}{2} \times \frac{M_{L,R}}{\phi_{1/2}} + \frac{1 - M^2_{r,1/2}}{2} \times \frac{M_{R,L}}{\phi_{1/2}}, \tag{29}$$

  where $M_r^2 = c'^2/c^2$ with the same c' in Eq. (11) and

$$\phi_{1/2} = \frac{\sqrt{(1 - M^2_{r,1/2})M^2_{1/2} + 4M^2_{r,1/2}}}{1 + M^2_{r,1/2}}.$$

  The interfacial speed of sound in Eq. (13) was replaced by the scaled speed of sound:

$$c^*_{1/2} = c_{1/2} \times \phi_{1/2}. \tag{30}$$

  In order to prevent the odd-even decoupling problem in the low Mach number regime, the pressure-based weight function was scaled as:

$$f^* = f \times \frac{1}{M_r^2}. \tag{31}$$

3.3 AUSMPW+_N for Cryogenic Multi-phase Mixture Flows

Although it was confirmed that the above two-phase AUSMPW+ was robust and efficient for gas-liquid two-phase flows, the application area was limited because the two-phase SDST was dependent on a specific form of EOS (i.e., stiffened-gas model for liquid). In addition, the two-phase AUSMPW+ could not guarantee the accuracy for unsteady low Mach number flows, as it did not take into account unsteady preconditioning and corresponding flux scaling. Recently, more extended AUSMPW+_N was developed [12, 23]; there was no restriction on the choice of EOS model and proper scaling for unsteady low Mach number flows was included.

- **New SDST for general EOS**
  When a general EOS such as a tabular form of NIST database for a cryogen is incorporated into a flow solver, the two-phase AUSMPW+ cannot be employed because the term p_c inside the two-phase SDST (Eq. (26)) can be obtained only from a few types of EOS models. By exploiting the steady one-dimensional shock relations, a new SDST was designed as follows:

$$\Pi^*_{1/2} = \min\left(\frac{\bar{p}^*_L}{\bar{p}^*_R}, \frac{\bar{p}^*_R}{\bar{p}^*_L} \right), \quad \bar{p}^*_{L,R} = p_{L,R} + 0.1 \times \min\left(\rho_L c_L^2, \rho_R c_R^2 \right). \tag{32}$$

The newly introduced Π^* only requires the mixture density and speed of sound across a cell-interface which can be defined without a specific form of EOS. Then, the pressure-based weight functions become

$$f^*_{L,R} = \left(\frac{p_{L,R} + \rho_{1/2} c^2_{1/2}}{\rho_{1/2} c^2_{1/2}} - 1 \right) \times (1 - \omega^*) \times \frac{\rho_{1/2}}{\rho_{L/R}}, \quad \omega^* = \max(\omega^*_1, \omega^*_2), \tag{33}$$

with

$$\omega^*_1 = 1 - (\Pi^*_{1/2})^3, \quad \omega^*_2 = 1 - \left(\frac{\min(\bar{p}^*_{L+1}, \bar{p}^*_{R+1}, \bar{p}^*_{L-1}, \bar{p}^*_{R-1})}{\max(\bar{p}^*_{L+1}, \bar{p}^*_{R+1}, \bar{p}^*_{L-1}, \bar{p}^*_{R-1})} \right)^2.$$

- **Scaling for unsteady low Mach number flows**
  For unsteady low Mach number flows, the pressure and velocity difference dissipation terms need to be separately scaled, contrary to the steady low Mach number flows which can be handled by a uniform scaling technique. The scaling functions for the pressure and velocity difference terms were respectively given by

$$\phi_p = \theta_p(2 - \theta_p), \quad \theta_p = \min \left(1, \max \left(\frac{\sqrt{u^2_{1/2} + v^2_{1/2}}}{c_{1/2}}, \frac{V_{co}}{c_{1/2}}, \frac{V_{un}}{c_{1/2}} \right) \right), \tag{34}$$

  and

$$\phi_u = \theta_u(2 - \theta_u), \quad \theta_u = \min \left(1, \max \left(\frac{\sqrt{u^2_{1/2} + v^2_{1/2}}}{c_{1/2}}, \frac{V_{co}}{c_{1/2}} \right) \right). \tag{35}$$

  The AUSMPW+_N then modified the pressure flux Eq. (14) by adding the scaled velocity difference term as follows:

$$p_s = \mathscr{P}^+_L p_L + \mathscr{P}^-_R p_R - 2K_u \mathscr{P}^+_L \mathscr{P}^-_R \rho_{1/2} c_{1/2} \phi_u (U_R - U_L), \tag{36}$$

  with $0 \le K_u \le 1$. Next, the pressure difference term was scaled as

$$f^*_{L,R} = \frac{1}{\phi_p} \left(\frac{p_{L,R} + \rho_{1/2} c^2_{1/2}}{\rho_{1/2} c^2_{1/2}} - 1 \right) \times (1 - \omega^*) \times \frac{\rho_{1/2}}{\rho_{L/R}}. \tag{37}$$

  It is noted that the complex scaled Mach number (Eq. (29)) and scaled speed of sound (Eq. (30)) were discarded and the original Mach number and speed of sound (Eq. (25)) were restored.

3.4 Evaluation of AUSMPW+_N

The improved features in the AUSMPW+_N are tested in comparison with its predecessor.

- **The effect of SDST in the shock and water column interaction problem**
  In order to examine the changes in behavior of AUSMPW+_N caused by the choice of SDST (the original SDST from gas dynamics (Π^o), the two-phase SDST (Π), and the new SDST (Π^*)), a shock in gas impacting a water column was simulated. The problem's description is provided in Sect. 5.2. Figure 2 plots the inverse values of SDST at $t = 8\ \mu s$, where the shock passes the middle of the water column. The original SDST and two-phase SDST misinterpreted the vicinity of the phase interface as the shock region; the inverse of SDST was even higher than the gaseous shock. Eventually, inaccurate numerical dissipation across the phase interface made the computations fail. On the contrary, the new SDST, $\Pi^*_{1/2}$, successfully sensed the shock discontinuity without confusing it with the circular phase interface. Here, we assume pure liquid and pure gas phases, but if a small volume fraction of gas (10^{-5}) was put in the water column, and vice versa, all three SDSTs pass the test without difficulty.

- **The effect of unsteady scaling functions in a low Mach unsteady problem**
  The propagation of an inviscid vortex in a low Mach number flow ($M_\infty = 0.005$) was computed. The detailed problem definition and the discussion of the computed results are found in Kim *et al.* [12]. The

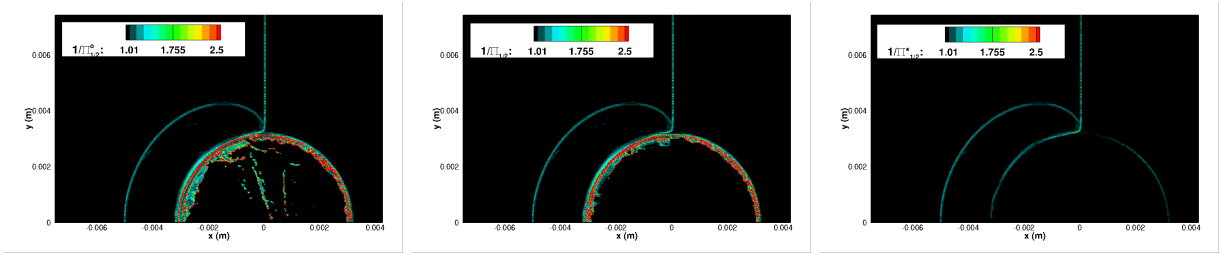

(a) $1/\Pi^{o}_{1/2}$ (b) $1/\Pi_{1/2}$ (c) $1/\Pi^{*}_{1/2}$

Figure 2: Inverse values of SDST in the shock and water column interaction problem

simultaneous enhancement of the accuracy and efficiency of the AUSMPW+_N is briefly shown in Fig. 3. Since the previous two-phase AUSMPW+ scheme cannot handle the velocity and pressure difference dissipation terms separately, the improved accuracy due to the steady preconditioning accompanies the degradation of subiteration convergence, and the accelerated convergence due to the unsteady preconditioning creates the diminished accuracy.

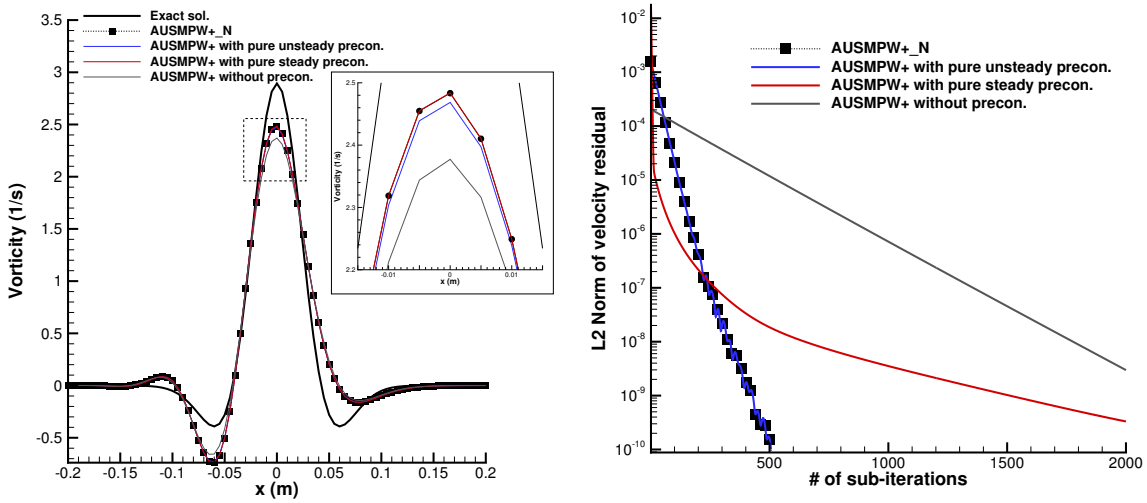

(a) Centerline vorticity at $t = 0.2304\ s$ (b) Subiteration convergence

Figure 3: Accuracy and convergence by different preconditioning methods

Hereafter, we only consider the AUSMPW+_N scheme on the grounds of its superiority.

4 An Interface Sharpening Procedure with Mass Conservation

In order to manage the diffusion of phase interfaces, Kinzel *et al.* [18] incorporated the reinitialization stage of the level-set method to the two-phase homogeneous mixture equations. They suggested three options for the reinitialization of the interface. LS-1 and LS-2 inherit the reinitialization technique used in the level-set community, but LS-3 is uninvolved with the conventional level-set method. The LS-3 strategy artificially scales the volume fraction in the interfacial mixture zone and thus does not require extra PDE to be solved, unlike the other two options. We have focused on the LS-3 scheme to preserve the main advantage of the homogeneous mixture model, which is its compact set of governing equations. While the application of LS-3 enhanced the quality of interface capturing, it was not mass-conservative. We adopted the idea of LS-3, and modified it to be mass-conservative as well as extended the scheme to a three-component situation.

4.1 LS-3: Realizable-Scaled Sharpening

Before presenting our extension, here is the original realizable-scaled sharpening method (LS-3) [18], which utilizes the following equation to scale the volume fraction.

$$\alpha^* = \min\left(\max\left(\frac{1}{2}\left[\frac{\alpha^{n+1/2} - 0.5}{0.5 - \epsilon} + 1\right], 0\right), 1\right) \text{ with } 0 \le \epsilon < 0.5. \tag{38}$$

We followed the popular notation of gaseous volume fraction α and confined our interest to a two-phase flow of liquid and gas. The intermediate volume fraction $\alpha^{n+1/2}$ is obtained by solving the flow equations (Eq. (1)) and the fluid properties at the next time step $(n+1)$ are updated by the scaled volume fraction $\alpha^{n+1} = \alpha^*$. Independent of the local cell size, the parameter ϵ determines the sharpness of the scaled volume fraction. Figure 4(a) shows the relationship between $\alpha^{n+1/2}$ and α^*. The application of LS-3 to a smeared interface is demonstrated in Fig. 4(b). The baseline volume fraction profile was obtained by solving $\frac{\partial \alpha}{\partial t} + u\frac{\partial \alpha}{\partial t} = 0$ with the 1st-order upwind method. The initial discontinuous profile ($\alpha = 0$ for $x < 0.1$, $\alpha = 1$ for $x \ge 0.1$) was smeared at $t = 2$ with $u = 0.05$. The reconstructed profile was sharper with larger ϵ. In actual computations, the reconstruction procedure was practiced with a sharpening frequency f_{ls}. To improve numerical stability, a relaxation was applied as follows:

$$\alpha^{n+1} = \alpha^* + f_r(\alpha^{n+1/2} - \alpha^*).$$

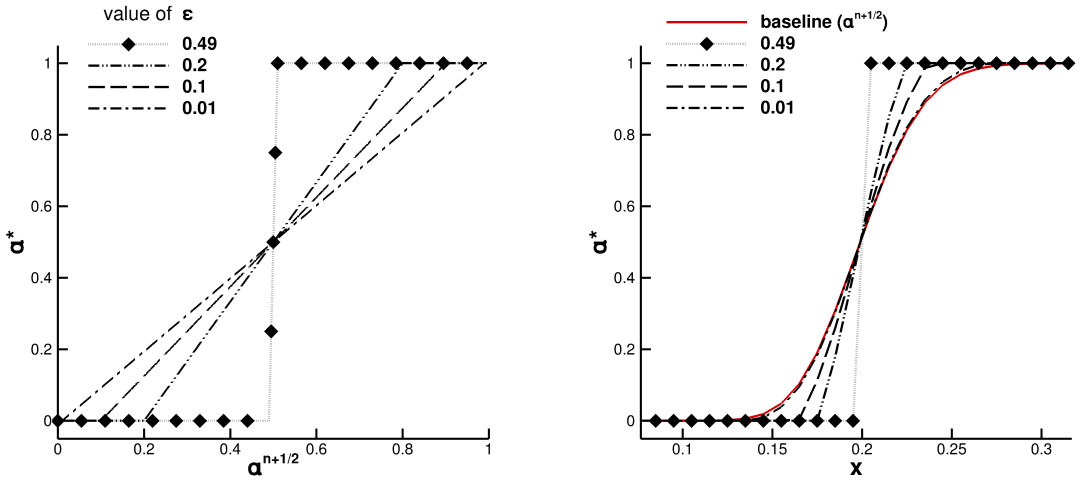

(a) Relation between $\alpha^{n+1/2}$ and α^*

(b) Reconstructed α using LS-3

Figure 4: Reconstruction of volume fraction by LS-3

4.2 LS-3MC: Realizable-Scaled Sharpening with Mass Conservation

Even though the governing equations are in a conservative form and solved by a conservative method, they could fail to satisfy mass conservation when implemented with the LS-3 scheme. The mass change comes from the fixed interface-defining level set ($\alpha = 0.5$) in Eq. (38). We propose the realizable-scaled sharpening with mass conservation scheme (LS-3MC) which maintains the global mass of the system after reinitialization.

$$\alpha^* = \min\left(\max\left(\frac{1}{2}\left[\frac{\alpha^{n+1/2} - \alpha_{ref}}{0.5 - \epsilon} + 2\alpha_{ref}\right], 0\right), 1\right) \text{ with } 0 \le \epsilon < 0.5. \tag{39}$$

The interface-defining level set α_{ref} is newly determined each time Eq. (39) is computed according to f_{ls}. Once α_{ref} is determined for a certain time, it is applied to the entire cells.

The mass-conserving value of α_{ref} can be always determined, which is demonstrated as follows. Let M_o be the baseline mass with a smeared interface as the solution of the flow equations. The mass after reconstruction, M_r, is a function of α_{ref}, or $M_r(\alpha_{ref})$, since ρ_l and ρ_g of a cell are constants at $(n+1/2)$ time (of course, they may differ in other cells). When the liquid density is higher than the gas, the smallest possible M_r is $M_r(\alpha_{ref}=0)$ with $\epsilon \to 0.5$, which corresponds to a situation where the entire interfacial mixture zone is filled by the pure gas phase (Fig. 5(a)). Conversely, the largest possible M_r is derived when the mixture zone is filled by the pure liquid phase (Fig. 5(c)). In an actual baseline situation with a smeared interface, the "mixture" zone is filled by a mix of heavy liquid and light gas (Fig. 5(b)). Therefore, the following is valid.

$$M_r(\alpha_{ref}=0) \le M_o \le M_r(\alpha_{ref}=1) \tag{40}$$

From the intermediate value theorem, α_{ref} satisfying $M_r(\alpha_{ref}) = M_o$ always exists.

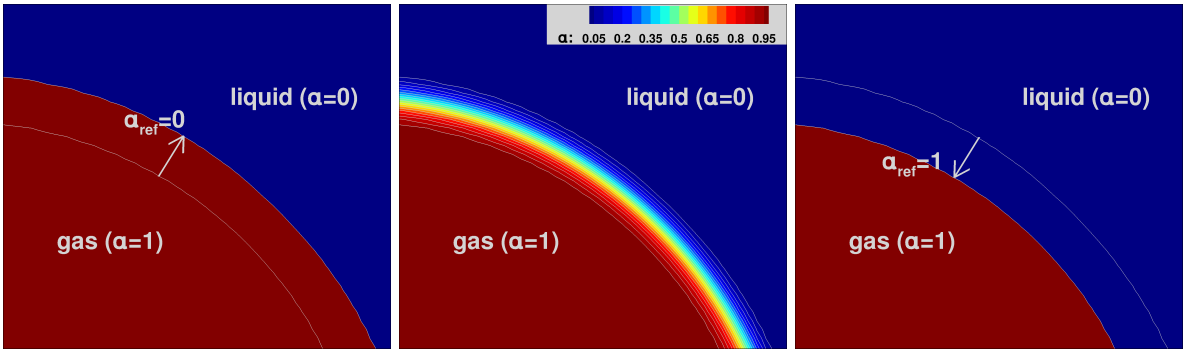

(a) Possible minimum M_r (b) M_o (c) Possible maximum M_r

Figure 5: M_o and the limits of M_r

Figure 6 shows the reconstructed volume fraction by LS-3MC from the same baseline profile used in Fig. 4(b). Depending on the value of α_{ref}, the position of the reconstructed interface is shifted. Table 1 shows the M_r in the case of $\epsilon = 0.2$ when $\rho_l = 1000$ and $\rho_g = 10$ in a one-dimensional domain $(-0.5, 1.5)$. The mass-preserving α_{ref} is deduced to be a value between 0.5 and 0.8 and can be determined by the iterative process. It is noted that the iterative process for finding the precise value of α_{ref} is conducted once for the entire system, not for each individual cell, since the LS-3MC method reconstructs the cell-representative values, not the sub-cell distributions.

Table 1: Total mass after reconstruction with different α_{ref}

M_o	713.00				
α_{ref}	0	0.2	0.5	0.8	1
M_r	650.82	702.63	712.25	722.22	730.73

The overall procedure with the LS-3MC is outlined as follows:

– Step 1: Solve the flow governing equations using Eq. (1). When the time step, n, corresponds to $N \times 1/f_{ls}$ (in which N is a positive integer), proceed to Step 2 after updating the flow variables of the intermediate time step.

– Step 2: From the solution of flow equations, obtain M_o and $\alpha^{n+1/2} = (\rho^{n+1/2} y_g^{n+1/2})/\rho_g^{n+1/2}$.

– Step 3: With an initial α_{ref}=0.5, calculate α^* using Eq. (39).

– Step 4: Compare M_o and $M_r(\alpha^*)$.

- If $M_r(\alpha^*) > M_o$, reduce the value of α_{ref} based on an iterative method and return to Step 3.
- If $M_r(\alpha^*) < M_o$, raise the value of α_{ref} and repeat from Step 3.

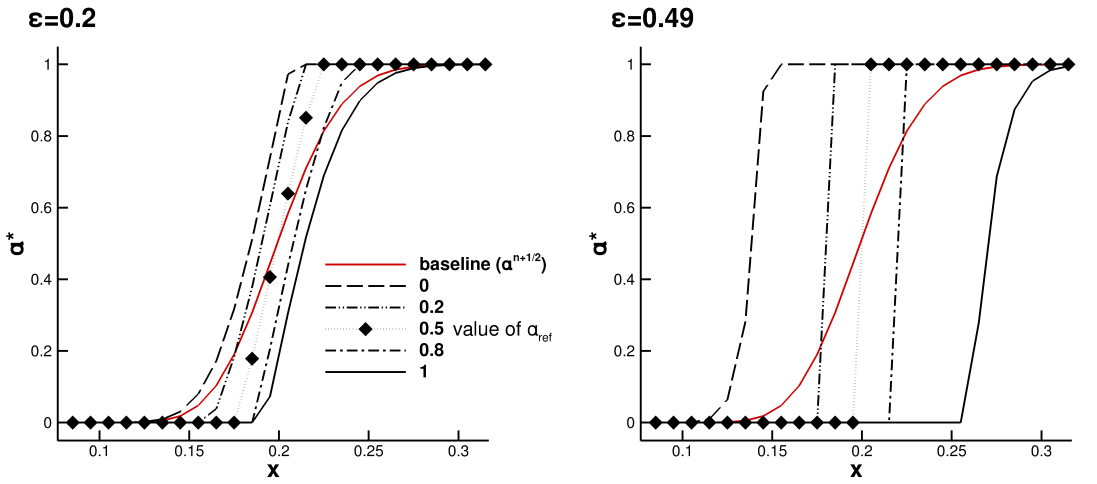

(a) Reconstructed α using LS-3MC with $\epsilon = 0.2$

(b) Reconstructed α using LS-3MC with $\epsilon = 0.49$

Figure 6: Reconstruction of volume fraction by LS-3MC

- If $M_r(\alpha^*) = M_o$, go to Step 5.

– Step 5: Set α^{n+1} as α^* and update the mixture density, mass fractions, and mixture enthalpy. The density and enthalpy of each phase remain constant throughout Steps 2−5 since p and T do not change; only the mixture properties are changed by the reconstruction of the volume fraction.

$$\begin{aligned}\rho^{n+1} =& \alpha^{n+1}\rho_g^{n+1/2} + (1-\alpha^{n+1})\rho_l^{n+1/2}\\ y_g^{n+1} =& \alpha^{n+1}\rho_g^{n+1/2}/\rho^{n+1}\\ h^{n+1} =& y_g^{n+1}h_g^{n+1/2} + \left(1-y_g^{n+1}\right)h_l^{n+1/2}\end{aligned}$$

The essential steps in the LS-3MC compute the global mass and the scaling of cell-representative volume fractions by Eq. (39). These calculations are performed in an identical manner in 1-, 2-, and 3-D flow solvers and are free from any geometric constraint. Therefore, the LS-3MC procedure can be incorporated into a flow solver for multi-phase mixture, irrespective of the physical dimension and mesh type (structured or unstructured).

4.3 Utilization of Smooth Curves

In Figs. 4 and 6, some reconstructed profiles seem non-differentiable near α=0 or 1. The non-smooth reconstruction is a result of min and max cutting in Eqs. (38) and (39). This is not a problem for the purpose of interface sharpening, but may yield potential difficulty when computing the gradient of the volume fraction in situations such as those where the surface tension must be considered. We employ a smooth reconstruction using the tanh function as follows:

$$\alpha^* = \frac{\tanh(\alpha_{ref}/\epsilon) + \tanh\left((\alpha^{n+1/2} - \alpha_{ref})/\epsilon\right)}{\tanh(\alpha_{ref}/\epsilon) + \tanh\left((1-\alpha_{ref})/\epsilon\right)}. \tag{41}$$

The THINC method [15] also takes advantage of the tanh function, but it reconstructs the sub-cell distribution of fluid properties for flux computation. Another smooth reconstruction is embodied using the Bézier curve with 11 control points designed for a nice curve.

$$\alpha^* = \Sigma_{i=0}^{10} b_{i,10}(t) P_i \tag{42}$$

with

$$t = \begin{cases} 1 & \text{if } \alpha^{n+1/2} > 1-\epsilon \\ 0 & \text{if } \alpha^{n+1/2} < \epsilon \\ \frac{1}{2}\left(\frac{\alpha^{n+1/2}-0.5}{0.5-\epsilon}+1\right) & \text{else} \end{cases},$$

$$b_{i,10} = \frac{10!}{i!(10-i)!}t^i(1-t)^{10-i} \quad (i = 0, ..., 10),$$

$$P_i = \begin{bmatrix} 0 \\ 0 \\ \alpha_{ref}-0.23 \\ \alpha_{ref}-0.2 \\ \alpha_{ref}-0.15 \\ 0.5 \\ \alpha_{ref}+0.15 \\ \alpha_{ref}+0.2 \\ \alpha_{ref}+0.23 \\ 1 \\ 1 \end{bmatrix}.$$

Compared to the linear reconstruction (Eq. (39)) the formulations for smooth curves are more complex, but computational overload is negligible because f_{ls} is typically $10^{-3} - 10^{-4}$. Moreover, the goal of the LS-3MC method is to conserve the total mass; thus, a computation for the entire system is sufficient and cell by cell computations are unnecessary and, in fact, impossible.

4.4 Extension to a Three-Component Situation

So far, we have confined our discussion to a two-phase flow of liquid and gas, but the extension of the LS-3MC to a three-component situation is straightforward due to the simplicity of the scheme. For a multi-phase flow consisting of L (the liquid phase of a fluid), V (the gas phase of the same fluid), and G (the non-condensable gas of another fluid), the LS-3MC method is applied twice in successive manner.

- Apply LS-3MC to the mixture of L and (V+G) following Steps 1−5 in Sect. 4.2 to sharpen the interface adjacent to the L phase. Here, $\alpha_1^{n+1/2} = \alpha_v^{n+1/2} + \alpha_g^{n+1/2}$ is considered as α in Eq. (39). Step 2 is slightly modified to be:

  – Step 2: Obtain M_o, $\alpha_1^{n+1/2} = \rho^{n+1/2}\left(y_v^{n+1/2}/\rho_v^{n+1/2} + y_g^{n+1/2}/\rho_g^{n+1/2}\right)$, and $q^{n+1/2} = \alpha_g^{n+1/2}/\alpha_1^{n+1/2}$.

  The volume fraction ratio of G to the mixture of gases (V+G) is for computing the total density after reconstruction. We assume that the scaling of α consistently applies to α_v and α_g. After finding the mass-conserving α_{ref}, the updated variables in Step 5 are marked as (n+1*) state.

  – Step 5: Set α_1^{n+1*} as α^* and compute the volume fraction of each phase at $(n+1*)$.

$$\begin{aligned} \alpha_g^{n+1*} &= \alpha_1^{n+1*} q^{n+1/2} \\ \alpha_v^{n+1*} &= \alpha_1^{n+1*}(1-q^{n+1/2}) \end{aligned}$$

- Apply LS-3MC again to the mixture of V and G from Step 2, keeping α_1^{n+1*} constant. In order to use the same code to find the mass-conserving α_{ref} as the first reconstruction, the total volume fraction of the V and G mixture is regarded as a unity during Steps 2−4. Thus, α_2^{n+1*}, the relative volume fraction of the lighter phase between V and G, is used as α in Eq. (39).

  – Step 2: Obtain M_o and $\alpha_2^{n+1*} = \alpha_g^{n+1*}/(\alpha_v^{n+1*} + \alpha_g^{n+1*}) = \alpha_g^{n+1*}/\alpha_1^{n+1*}$.

After finding the mass-conserving α_{ref}, the variables are updated to the next time step (n+1).

– Step 5: Set α_2^{n+1} as α^* and update the mixture density, mass fractions, and mixture enthalpy.

$$
\begin{aligned}
\rho^{n+1} =& \alpha_1^{n+1*}\rho_{(v+g)}^{n+1} + (1-\alpha_1^{n+1*})\rho_l^{n+1/2} \\
=& \alpha_1^{n+1*}[\alpha_2^{n+1}\rho_g^{n+1/2} + (1-\alpha_2^{n+1})\rho_v^{n+1/2}] + (1-\alpha_1^{n+1*})\rho_l^{n+1/2} \\
y_g^{n+1} =& \alpha_g^{n+1}\rho_g^{n+1/2}/\rho^{n+1} = \alpha_1^{n+1*}\alpha_2^{n+1}\rho_g^{n+1/2}/\rho^{n+1} \\
y_v^{n+1} =& \alpha_v^{n+1}\rho_g^{n+1/2}/\rho^{n+1} = \alpha_1^{n+1*}(1-\alpha_2^{n+1})\rho_v^{n+1/2}/\rho^{n+1} \\
h^{n+1} =& y_g^{n+1}h_g^{n+1/2} + y_v^{n+1}h_v^{n+1/2} + \left(1-y_g^{n+1}-y_v^{n+1}\right)h_l^{n+1/2}
\end{aligned}
$$

5 Numerical Results

Various multi-phase flows were considered to exhibit the performance of the present numerical framework. Compressible problems with shock and phase interface demonstrated the robustness of the AUSMPW+_N for multi-phase shock and the effectiveness of the LS-3MC. The LS-3MC scheme was further tested by 2-D and 3-D interface-only problems. Finally, the flow inside a cryogenic tank under the injection of non-condensable gas was computed. This test revealed the applicability of the present numerical framework with the LS-3MC to three-component phase change flow. The MLP5 limiter [28] was used for all computations and the third-order TVD Runge-Kutta scheme [29] was adopted for temporal discretization unless stated otherwise.

5.1 Air-to-Water Shock Tube

First, a one-dimensional air-to-water shock tube problem was solved as a simple test for a two-phase compressible flow with shock and moving contact discontinuity. Due to the high density ratio, a large pressure difference is necessary to transmit the shock from air to water. The initial conditions are defined as:

$$
\begin{aligned}
\vec{Q}_L =& (1.0\times10^9 \text{ Pa},\ 0 \text{ m/s},\ 0 \text{ m/s}, 308.15 \text{ K},\ 0,\ y_{g,L}) \quad \text{for } 0 \text{ m} \le x \le 5 \text{ m}, \\
\vec{Q}_R =& (1.0\times10^5 \text{ Pa},\ 0 \text{ m/s},\ 0 \text{ m/s}, 308.15 \text{ K},\ 0,\ y_{g,R}) \quad \text{for } 5 \text{ m} < x \le 10 \text{ m}.
\end{aligned}
$$

Here, $y_{g,L}$ and $y_{g,R}$ are gas mass fractions that correspond to $\alpha_g = 1-\epsilon_\alpha$ and $\alpha_g = \epsilon_\alpha$, respectively. We set $\epsilon_\alpha = 1\times10^{-7}$. The parameters for the stiffened-gas EOS are $\gamma_g = 1.4$, $p_{\infty,g} = 0$, $C_{p,g} = 1004.64$ J/(kg · K), and $\gamma_l = 2.8$, $p_{\infty,l} = 8.5\times10^8$ Pa, $C_{p,l} = 4186$ J/(kg · K). A uniform grid of 500 cells was used with CFL=0.2. Figure 7(a) shows the results of volume fraction and pressure at $t = 2\times10^{-3}$ s. A strong shock is transmitted into the water and rarefaction waves are reflected back into the air. The AUSMPW+_N scheme captures the shock, phase interface, and rarefaction waves without any noticeable oscillation. In particular, the baseline AUSMPW+_N scheme captures the shock with $4-5$ grid points, but the contact discontinuity was captured with 10 points. The efficacy of the LS-3MC process (using the linear reconstruction with $f_{ls} = 0.01, \epsilon = 0.2$) is demonstrated in Fig. 7(b). With the LS-3MC scheme, the number of grid points in the mixture zone was reduced to 3.

5.2 Interaction between the Shock and the Water Column

As a more complex compressible two-phase problem, the interaction between a shock in air and a water column was computed. A cylindrical water column centered at the origin was struck by a moving air shock

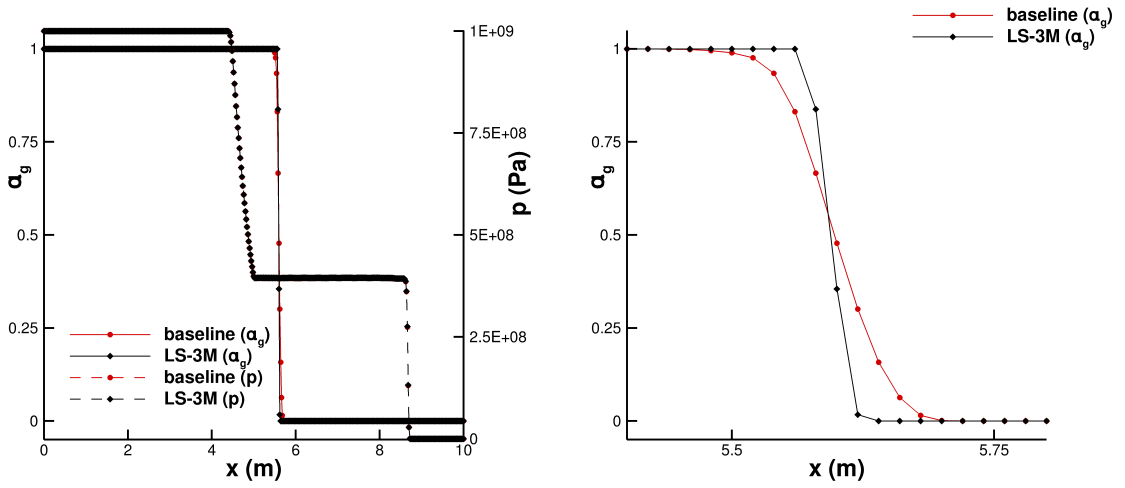

(a) Volume fraction and pressure

(b) Volume fraction (magnified)

Figure 7: Solutions of the air-to-water shock tube problem

of $M_s = 1.47$.

$$\vec{Q}_L = (2.35348 \times 10^5 \text{ Pa},\ 225.86 \text{ m/s},\ 0 \text{ m/s}, 381.85 \text{ K},\ 0,\ 1) \quad \text{for } -15 \text{ mm} \le x \le -4 \text{ mm},$$
$$\vec{Q}_R = (1.0 \times 10^5 \text{ Pa},\ 0 \text{ m/s},\ 0 \text{ m/s}, 293.15 \text{ K},\ 0,\ 1) \quad \text{for } -4 \text{ mm} < x \le 20 \text{ mm},$$
$$\vec{Q}_{\text{water}} = (1.0 \times 10^5 \text{ Pa},\ 0 \text{ m/s},\ 0 \text{ m/s}, 293.15 \text{ K},\ 0,\ 0) \quad \text{for } x^2 + y^2 < 3.2 \text{ mm}.$$

Most studies that solved the same problem put a small amount of gas in the liquid region and vice versa [30, 31], but our computations were carried out with pure liquid and gas phases for a more severe test. The same EOS parameters were used as in Sect. 5.1. The grid consisted of total 450×210 cells, which was refined to $\Delta x = \Delta y = 0.05$ mm near the water column and stretched outward. Computations were performed only for $y \ge 0$ and the symmetry condition was applied at the bottom boundary. At the water column interface, a transition region with a width of $\pm 2\Delta x_{\min}$ was specified by the blending function, which imposed a smooth change in the gas volume fraction across the phase interface. Computations were executed up to 200 μs with $\Delta t = 5 \times 10^{-9}$ s ($CFL \approx 0.3$).

Images of a numerical Schlieren function, $\log(|\nabla\rho| + 1)$, from the initial to the final time are presented in Fig. 8. The shock-discontinuity-sensing term in AUSMPW+_N worked as designed to distinguish the shock from the phase interface in two-phase flows. Intricate patterns of wave interactions inside the liquid are clearly captured by the AUSMPW+_N scheme (see [12] for pressure contours). The distortion of the water column and the evolution of Richtmyer-Meshkov instability were also properly simulated. At the beginning of the computations, the results for the high speed flows were very similar in the baseline and LS-3MC; thus, only the baseline results were included for $t = 20$ and 60 μs. At a later time, however, the incorporation of LS-3MC (using the Bézier curve reconstruction with $f_{ls} = 0.001, \epsilon = 0.1$) yielded quite a different result from the baseline. For this problem only, the LS-3MC method was applied to the interface cells detected by a filter $|\nabla\alpha_g| \ge 400$. Compared to Fig. 8(e), the darker contours around the water column in the baseline result indicates that the liquid mass is severely diffused and flows downstream along the shedding vortexes. For LS-3MC, the thin dark line is present only at the perimeter of the water column. The lighter color near the liquid indicates a lower density gradient due to a less diffused liquid mass. Figure 9 gives the contours of the volume fraction at $t = 100$ and 200 μs. The LS-3MC results retain a compact interface thickness without excessive smearing.

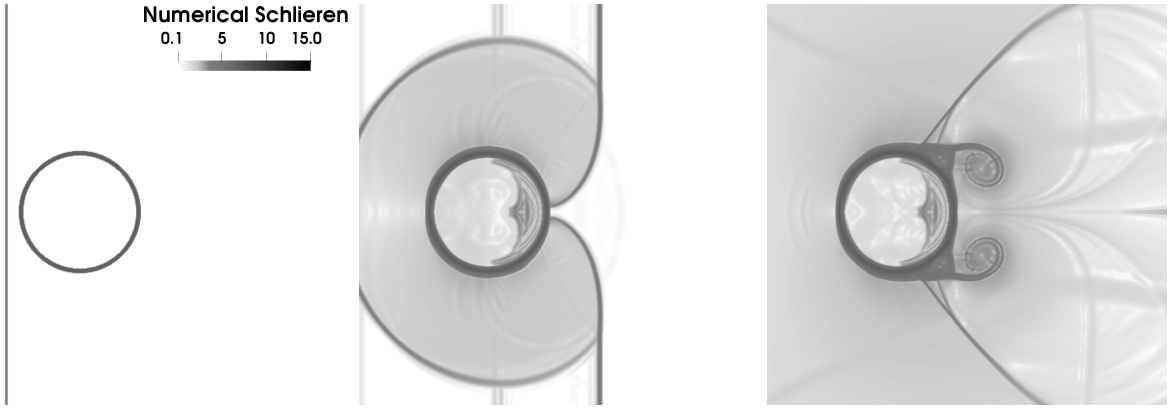

(a) $t = 0\ \mu s$ (b) Baseline at $t = 20\ \mu s$ (c) Baseline at $t = 60\ \mu s$

(d) Baseline at $t = 200\ \mu s$ (e) LS-3MC at $t = 200\ \mu s$

Figure 8: Numerical Schlieren images of the interaction between shock and water column problem

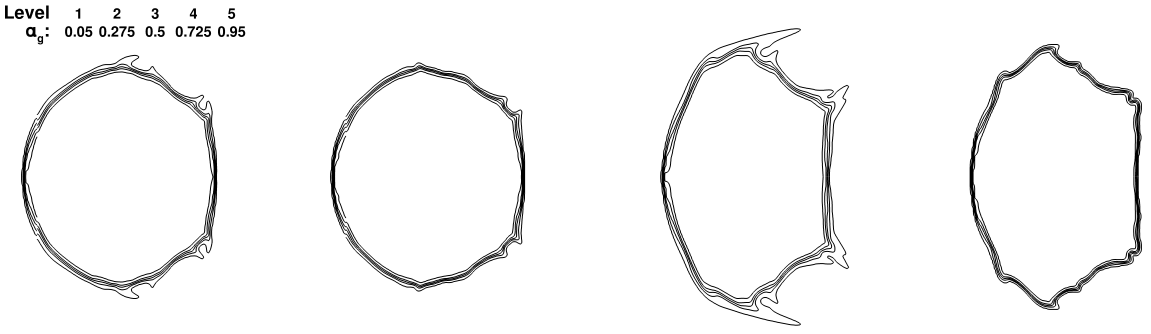

(a) Baseline at $t = 100\ \mu s$ (b) LS-3MC at $t = 100\ \mu s$ (c) Baseline at $t = 200\ \mu s$ (d) LS-3MC at $t = 200\ \mu s$

Figure 9: Contours of the volume fraction for the interaction between shock and water column problem

5.3 Translation of Square Liquid Column

This is a two-dimensional, interface-only problem. In a unit square domain, a square liquid column $[0.3, 0.7] \times [0.3, 0.7]$ m^2 in size was translated in gas with a constant velocity of $u = v = 100$ m/s, a uniform pressure

of $p = 10^5$ Pa, and a temperature of $T = 300$ K. The liquid region contained a small amount of gas ($\alpha_v = 10^{-8}$) and the gas region contained a small amount of liquid ($\alpha_l = 10^{-8}$). For this test, the fluid properties were modeled by the linearized Mie-Grüneisen EOS. If it was formulated as Eq. (5), the second term on the right-hand side ($-\gamma_i p_{\infty,i}$) became $c_{o,i}^2(\rho_i - \rho_{o,i})$. The required parameters were $\gamma_g = 1.4$, $c_{o,g} = 0$, $\rho_{o,g} = 1$ kg/m^3, $C_{p,g} = 1166.67$ J/(kg $\cdot$ K), and $\gamma_l = 4.4$, $c_{o,l} = 1624.8$ m/s, $\rho_{o,l} = 1000$ kg/m^3, $C_{p,l} = 0.4314$ J/(kg $\cdot$ K). A computational grid with uniform 100×100 cells was used, and a periodic boundary condition was applied for all sides. The computations were run for two periodic cycles.

Figure 10 shows contours of the mixture density after two-cycle run. For the purpose of comparison, the LS-3 method without mass conservation was also employed. The baseline solver results in a greatly smeared interface. The LS-3 method significantly reduces the interface diffusion, but fails to preserve the liquid mass (30 % of the initial mass is lost). On the other hand, the present LS-3MC method (using the tanh reconstruction with $f_{ls} = 0.0005$, $\epsilon = 0.2$) creates a sharpened interface without mass loss.

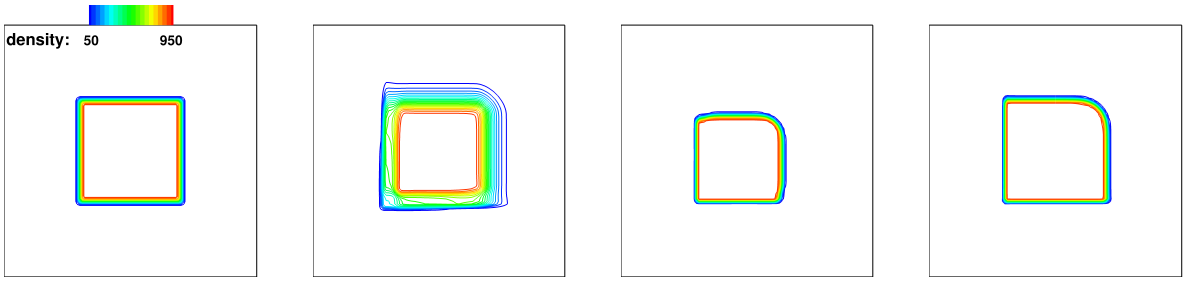

(a) $t = 0$ ms (b) Baseline at $t = 20$ ms (c) LS-3 at $t = 20$ ms (d) LS-3MC at $t = 20$ ms

Figure 10: Contours of the density after two-cycle run for the translation of square liquid column problem

In order to identify LS-3MC's quantitative improvement of accuracy, a grid refinement study was conducted (Table 2). The baseline solver was less than first-order accurate, but the order of accuracy was improved above first order when the solver was incorporated with the LS-3MC method. Due to the substantial mass loss, the LS-3 method shows the poorest accuracy.

Table 2: L^1 errors of the mixture density for the translation of square liquid column problem

N	Baseline		LS-3		LS-3MC (linear)		LS-3MC (tanh)		LS-3MC (Bézier)	
	Error	Order	Error	Order	Error	Order	Error	Order	Error	Order
50	52.2345	–	97.2752	–	30.8121	–	17.0809	–	31.8844	–
100	34.2274	0.61	50.6878	0.94	9.1400	1.75	8.6163	0.99	8.9092	1.84
200	21.5635	0.67	47.1270	0.11	3.8418	1.25	4.1648	1.05	4.1785	1.09
400	13.1488	0.71	45.7028	0.04	1.6917	1.18	1.9572	1.09	1.6788	1.32

5.4 Three-Dimensional Rising Bubble in Liquid

As stated before, the implementation of the LS-3MC process into a three-dimensional multi-phase flow solver is similar to the procedure for implementing into a two-dimensional solver. We further verified the effectiveness of LS-3MC in a three-dimensional, interface-only problem for a spherical bubble rising in liquid. Initially, a bubble of radius 0.005 m was located at the origin. Constant gravitational acceleration was applied ($\vec{g} = (0, 0, -9.8$ m/s^2)). Liquid and gas densities were set as 1000 and 10 kg/m^3, respectively. The computational domain $[-0.02, 0.02] \times [-0.02, 0.02] \times [-0.01, 0.09]$ m^3 was divided by $50 \times 50 \times 125$ uniform cubic cells, and the free-slip condition was applied for all boundaries. Since the entire flow field was incompressible, the dual time-stepping method with preconditioned LU-SGS [32] was used for time discretization. The CSF model [33] was also adopted to take surface tension into account.

When a spherical bubble rises in quiescent viscous liquid due to buoyancy, the rising speed and the bubble deformation are dependent on the dimensionless Morton number (Mo) and Eötvös number (Eo):

$$Mo = \frac{|g_z|\mu_l^4(\rho_l - \rho_g)}{\rho_l^2\sigma^3}, \quad Eo = \frac{|g_z|(\rho_l - \rho_g)d^2}{\sigma},$$

where μ_l, σ, d are the liquid viscosity, surface tension coefficient, and the bubble diameter, respectively. Grace [34] conducted extensive bubble rising experiments and integrated the results in a diagram that has been copied from Clift *et al.* [35] (Fig. 11). Here, we considered four cases witch similar Mo and Eo values as the study of van Sint Annaland *et al.* [36]. Conditions for the simulations are tabulated in Table 3, and each case is marked as a red dot in Grace's diagram in Fig. 11.

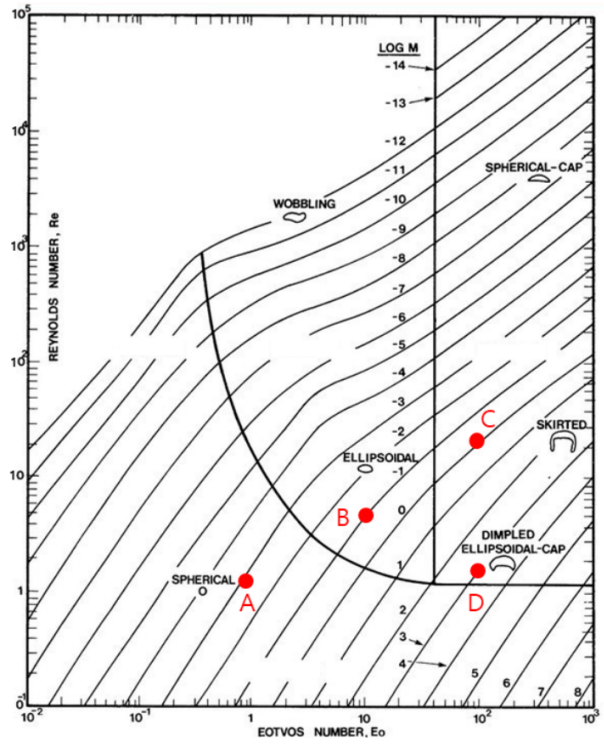

Figure 11: Bubble diagram of Grace [35]

Table 3: Conditions for the rising bubble simulations

	Case A	Case B	Case C	Case D
Bubble shape from Grace's diagram	Spherical	Ellipsoidal	Skirted	Dimpled ellipsoidal-cap
μ_l (kg/(m · s))	0.6	0.319	0.1	0.5666
σ (N/m)	1	0.1	0.01	0.01
Mo	1.26×10^{-3}	0.1	0.97	1000
Eo	0.971	9.709	97.09	97.09
Δt (s)	0.005	0.001	0.001	0.005
f_{ls}	1/6000	1/3000	1/3000	1/6000
ϵ	10^{-4}	10^{-3}	10^{-3}	10^{-2}

The baseline solver could not complete the simulations due to the excessive interface diffusion. As the interface became smeared, the bubble shape became distorted in an unexpected shape and the convergence

rate deteriorated due to the accumulated error. The computations of the baseline solver achieved awkward results (not presented here). The snapshots of iso-surface ($\alpha_g = 0.25$) computed by the LS-3MC method (the Bézier curve reconstruction) are given in Fig. 12. It can be seen that the deformed bubble shape matches Grace's diagram well, so the applicability of the LS-3MC scheme in three-dimensional computations was identified.

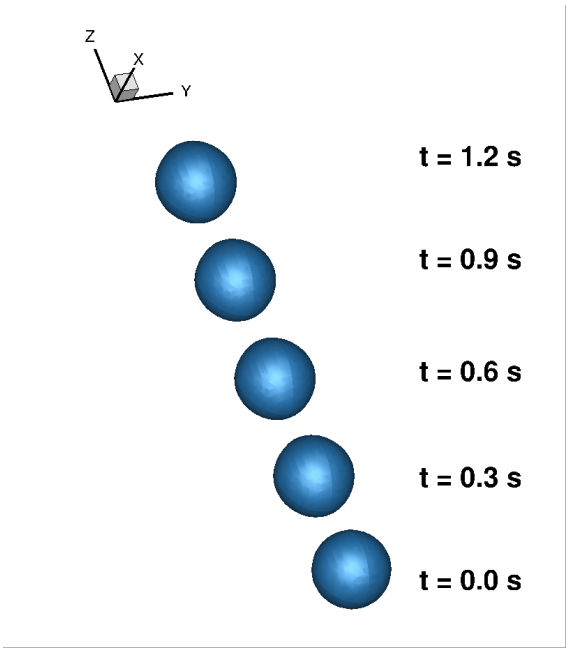

(a) Case A: spherical

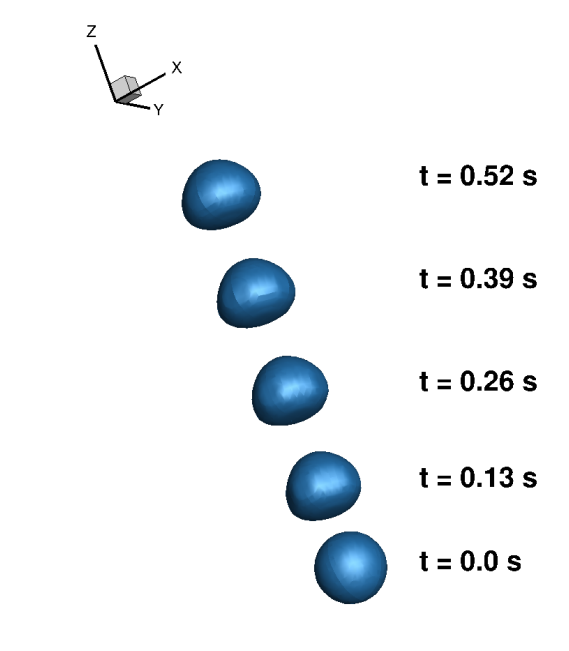

(b) Case B: ellipsoidal

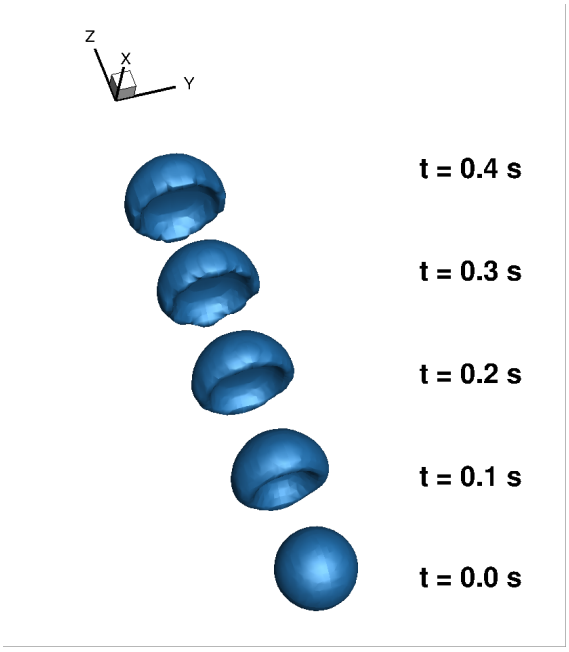

(c) Case C: skirted

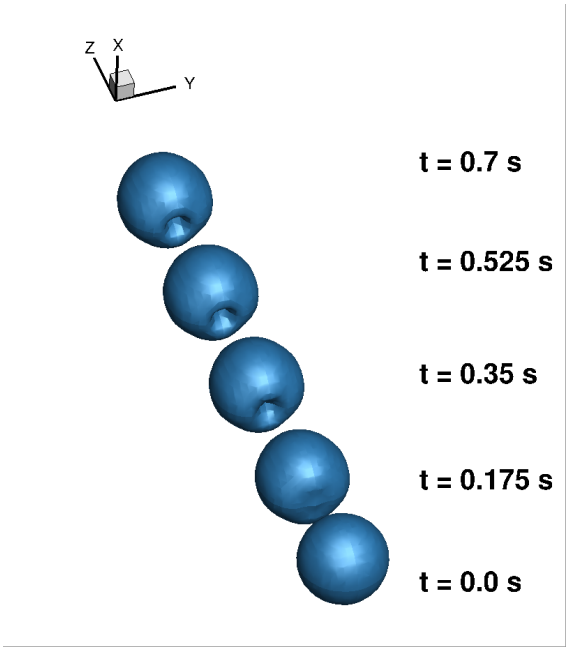

(d) Case D: dimpled ellipsoidal-cap

Figure 12: Iso-surface of $\alpha_g = 0.25$ of the rising bubble problem

Table 4: Initial conditions of the cryogenic tank simulation

	Fuel	Ullage	Pressurant
Initial fill level (%)	90	10	–
Fluid type	Liquid oxygen	Gaseous oxygen	Gaseous nitrogen
Temperature (K)	90.18	135.16	288
Pressure (MPa)	2.24	2.24	–

5.5 Phase Change Flow inside a Cryogenic Tank

As a test of the three-component flows, a phase change flow inside a cryogenic oxygen tank which is pressurized by the injection of superheated nitrogen gas was considered. The tank's geometry was taken from the E-1 high pressure LOX tank at NASA Stennis Space Center [37]. The initial conditions of the simulation are listed in Table 4. The pressurant gas entered radially through the diffuser at a mass flow rate of 453.64 kg/s. The effects of phase change and turbulence were modeled by the Merkle's model [38] and the $k-\omega$ SST model [39], respectively. The computational grid was composed of 26,000 cells. Since the AUSMPW+_N scheme is compatible with any type of EOS, a tabular form based on the NIST database was employed as EOS for cryogenic oxygen and nitrogen.

The results of the baseline and LS-3MC methods (using the linear reconstruction with $f_{ls} = 1/30000$, $\epsilon = 0.1$) are compared in Figs. 13 and 14. When the injection began at $t = 0$, the oxygen gas inside the tank and the injected nitrogen gas mixed and formed a vortex. The initially flat interface between the gas and liquid oxygen curled up along the vortex. Eventually, the oxygen gas, liquid, and nitrogen were completely mixed. The condensation of oxygen gas also occurred at the contact surface with liquid during the entire simulation. Since three phases exist inside the tank, the LS-3MC method was applied twice (see Sect. 4.4). Figure 13 shows the interface evolution between the injected nitrogen gas (shown in red) and others (the liquid and gaseous oxygen, both shown in blue). Figure 14 shows the interface evolution between the liquid oxygen (shown in red) and others (the gaseous oxygen and nitrogen, both shown in blue). The LS-3MC process successfully sharpens each intricately evolving interface in the three component flows where phase changes are occurring.

6 Conclusion

The extensions of AUSMP-type fluxes from compressible gas dynamics to all-speed multi-phase flows have been presented. The extended scheme, AUSMPW+_N, effectively modified the shock-discontinuity-sensing term to distinguish a shock from phase interfaces, irrespective of EOS type. The pressure-difference and the velocity-difference terms in the AUSMPW+_N scheme were separately scaled so that the accuracy and convergence were simultaneously satisfied for steady/unsteady low Mach number flows. The multi-phase computations by the AUSMPW+_N was further improved by employing an interface sharpening procedure. The proposed sharpening method simply scales the volume fractions while preserving the total mass of the system. Due to its simplicity, the method was extendable to multi-phase flows with more than two phases without much effort. From various multi-phase tests, it was confirmed that the diffused interfaces of the baseline solver regained the original sharpness regardless of the physical dimension, the number of constituent components, or the flow speed.

Acknowledge

This research was supported by the program of the National Space Laboratory (NRF-2014M1A3A3A02034856) and Advanced Research Center Program (NRF-2013R1A5A1073861) through the National Research Foundation of Korea grant funded by the Korea government contracted through Advanced Space Propulsion Research Center at Seoul National University.

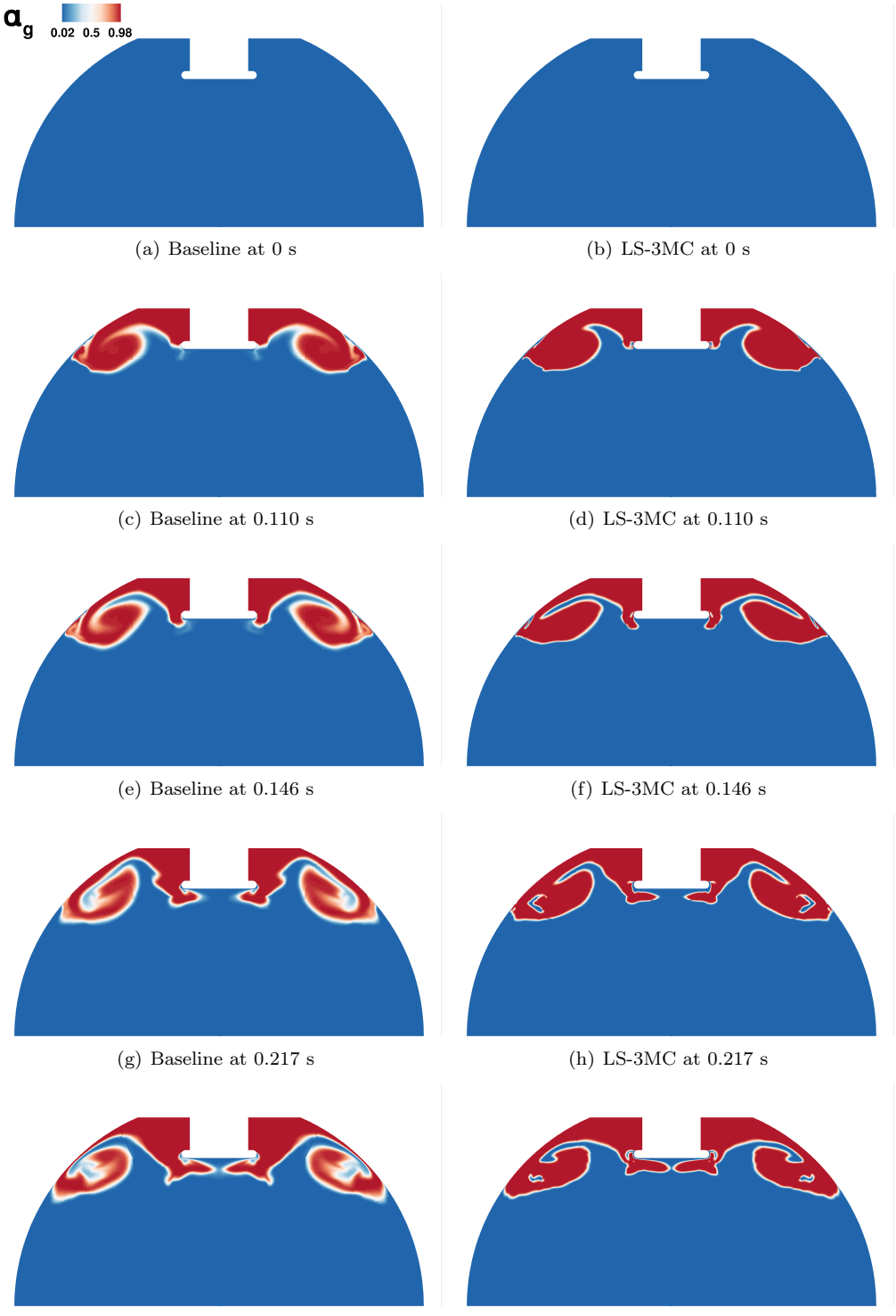

(a) Baseline at 0 s

(b) LS-3MC at 0 s

(c) Baseline at 0.110 s

(d) LS-3MC at 0.110 s

(e) Baseline at 0.146 s

(f) LS-3MC at 0.146 s

(g) Baseline at 0.217 s

(h) LS-3MC at 0.217 s

(i) Baseline at 0.288 s

(j) LS-3MC at 0.288 s

Figure 13: Evolution of non-condensable gas surface inside a cryogenic tank under the injection of pressurant

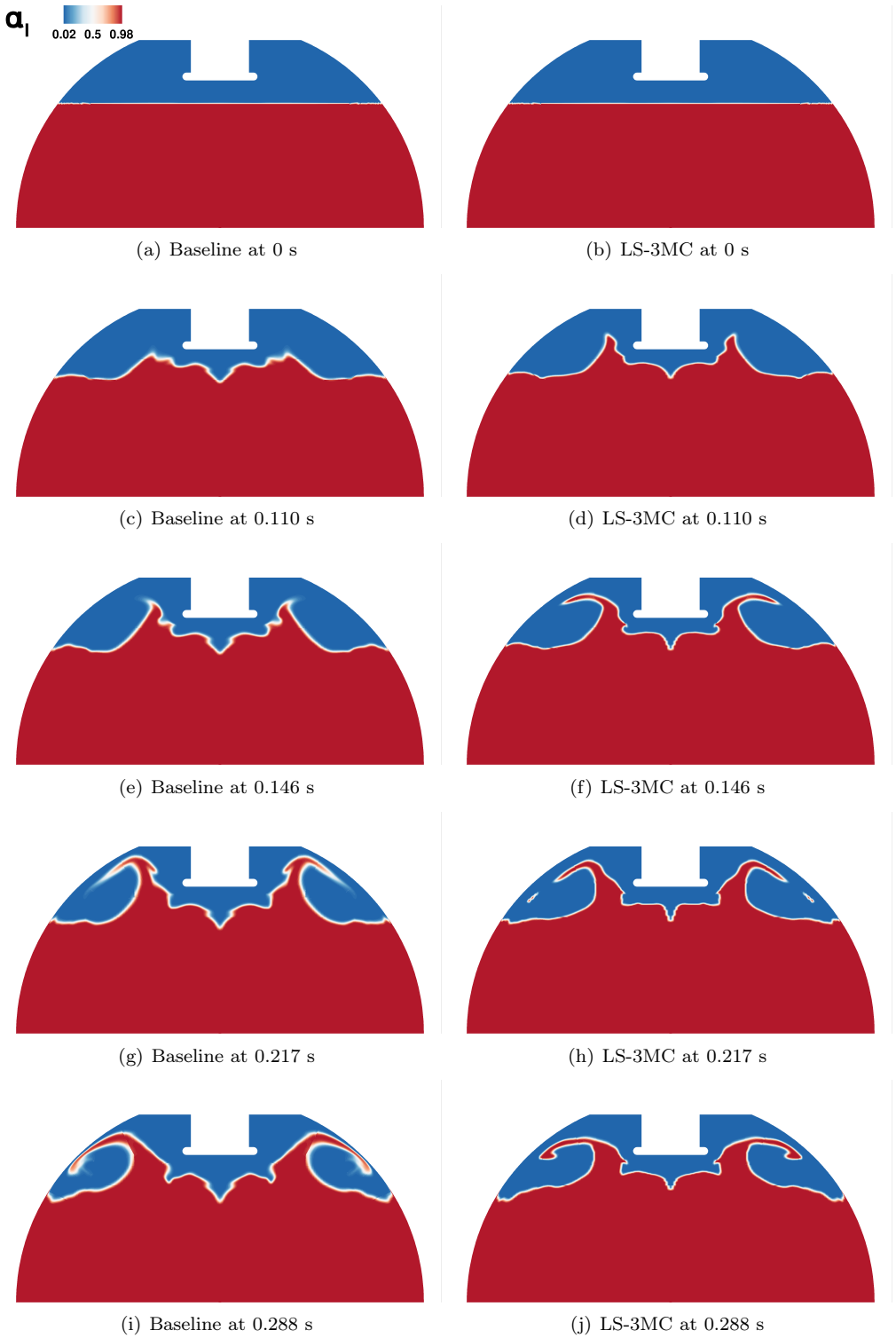

(a) Baseline at 0 s

(b) LS-3MC at 0 s

(c) Baseline at 0.110 s

(d) LS-3MC at 0.110 s

(e) Baseline at 0.146 s

(f) LS-3MC at 0.146 s

(g) Baseline at 0.217 s

(h) LS-3MC at 0.217 s

(i) Baseline at 0.288 s

(j) LS-3MC at 0.288 s

Figure 14: Evolution of liquid surface inside a cryogenic tank under the injection of pressurant

References

[1] G. Tryggvason, B. Bunner, A. Esmaeeli, D. Juric, N. Al-Rawahi, W. Tauber, J. Han, S. Nas, and Y. J. Jan. A Front-Tracking Method for the Computations of Multiphase Flow. *Journal of Computational Physics*, 169(2):708–759, 2001.

[2] S. Osher and J. A. Sethian. Fronts propagating with curvature-dependent speed: Algorithms based on Hamilton-Jacobi formulations. *Journal of Computational Physics*, 79(1):12–49, 1988.

[3] R. P. Fedkiw, T. Aslam, B. Merriman, and S. Osher. A Non-oscillatory Eulerian Approach to Interfaces in Multimaterial Flows (the Ghost Fluid Method). *Journal of Computational Physics*, 152(2):457–492, 1999.

[4] M. R. Baer and J. W. Nunziato. A two-phase mixture theory for the deflagration-to-detonation transition (DDT) in reactive granular materials. *Int. J. Multiphase Flow*, 12(6):861–889, 1986.

[5] A. K. Kapila, R. Menikoff, J. B. Bdzil, S. F. Son, and D. S. Stewart. Two-phase modeling of deflagration-to-detonation transition in granular materials: Reduced equations. *Physics of Fluids*, 13(10):3002–3024, 2001.

[6] R. Saurel and R. Abgrall. A Multiphase Godunov Method for Compressible Multifluid and Multiphase Flows. *Journal of Computational Physics*, 150(2):425–467, 1999.

[7] M.-S. Liou and C. J. Steffen. A new flux splitting scheme. *Journal of Computational Physics*, 107(1):23–39, 1993.

[8] M.-S. Liou. A sequel to AUSM: AUSM+. *Journal of Computational Physics*, 129:364–382, 1996.

[9] M.-S. Liou. A sequel to AUSM, Part II: AUSM+-up for all speeds. *Journal of Computational Physics*, 214(1):137–170, 2006.

[10] K. H. Kim, C. Kim, and O.-H. Rho. Methods for the Accurate Computations of Hypersonic Flows. *Journal of Computational Physics*, 174(1):38–80, 2001.

[11] S.-W. Ihm and C. Kim. Computations of Homogeneous-Equilibrium Two-Phase Flows with Accurate and Efficient Shock-Stable Schemes. *AIAA Journal*, 46(12):3012–3037, 2008.

[12] H. Kim, H. Kim, and C. Kim. Computations of Homogeneous Multiphase Real Fluid Flows at All Speeds. *AIAA journal*, 2018.

[13] R. K. Shukla, C. Pantano, and J. B. Freund. An interface capturing method for the simulation of multi-phase compressible flows. *Journal of Computational Physics*, 229(19):7411–7439, 2010.

[14] K. K. So, X. Y. Hu, and N. A. Adams. Anti-diffusion interface sharpening technique for two-phase compressible flow simulations. *Journal of Computational Physics*, 231(11):4304–4323, 2012.

[15] K.-M. Shyue and F. Xiao. An Eulerian interface sharpening algorithm for compressible two-phase flow: The algebraic THINC approach. *Journal of Computational Physics*, 268:326–354, 2014.

[16] A. Chiapolino, R. Saurel, and B. Nkonga. Sharpening diffuse interfaces with compressible fluids on unstructured meshes. *Journal of Computational Physics*, 340:389–417, 2017.

[17] C.-T. Ha, D.-H. Kim, W.-G. Park, and C.-M. Jung. A compressive interface-capturing scheme for computation of compressible multi-fluid flows. *Computers and Fluids*, 152:164–181, 2017.

[18] M. P. Kinzel, J. W. Lindau, and R. F. Kunz. A multiphase level-set approach for all-Mach numbers. *Computers and Fluids*, 167:1–16, 2018.

[19] NIST. NIST Reference Fluid Thermodynamic and Transport Properties Database (REFPROP): Version 8.0. [http://www.nist.gov/srd/nist23.cfm], 2010.

[20] IAPWS. Guideline on the Fast Calculation of Steam and Water Properties with the Spline-Based Table Look-Up Method (SBTL). Technical report, 2015.

[21] J. M. Weiss and W. A. Smith. Preconditioning applied to variable and constant density flows. *AIAA Journal*, 33(11):2050–2057, 1995.

[22] S. Venkateswaran and C. L. Merkle. Dual time-stepping and preconditioning for unsteady computations. *33rd Aerospace Sciences Meeting and Exhibit*, 1995.

[23] H. Kim, Y. Choe, H. Kim, D. Min, and C. Kim. Methods for compressible multiphase flows and their applications. *Shock Waves, in press*, 2018.

[24] Y. Wada and M.-S. Liou. A flux splitting scheme with high-resolution and robustness for discontinuities. *32nd Aerospace Sciences Meeting and Exhibit*, 1994.

[25] K. H. Kim, J. H. Lee, and O. H. Rho. An improvement of AUSM schemes by intrdoducing the pressure based weight functions. *Computers & Fluids*, 27(3):311–346, 1998.

[26] K. H. Kim and C. Kim. Accurate, efficient and monotonic numerical methods for multi-dimensional compressible flows. Part I: Spatial discretization. *Journal of Computational Physics*, 208(2):527–569, 2005.

[27] J. R. Edwards and M.-S. Liou. Low-diffusion flux-splitting methods for flows at all speeds. *AIAA Journal*, 36(9):1610–1617, 1998.

[28] S.-H. Yoon, C. Kim, and K.-H. Kim. Multi-dimensional limiting process for three-dimensional flow physics analyses. *Journal of Computational Physics*, 227:6001–6043, 2008.

[29] S. Gottlieb and C.-W. Shu. Total Variation Diminishing Runge-Kutta Schemes. *Mathematics of Computation*, 67(221):73–85, 1998.

[30] K. Kitamura and M.-S. Liou. Comparative Study of AUSM-Family Schemes in Compressible Multiphase Flow Simulations. *Iccfd7*, pages 1–25, 2012.

[31] T. Nonomura, K. Kitamura, and K. Fujii. A simple interface sharpening technique with a hyperbolic tangent function applied to compressible two-fluid modeling. *Journal of Computational Physics*, 258:95–117, 2014.

[32] S. Yoon and A. Jameson. Lower-Upper Symmetric-Gauss-Seidel Method for the Euler and Navier-Stokes Equations. *AIAA Journal*, 26(9):1025–1026, 1988.

[33] J. U. Brackbill, D. B. Kothe, and C. Zemach. A continuum method for modeling surface tension. *Journal of Computational Physics*, 100(2):335–354, 1992.

[34] J. R. Grace. Shapes and velocities of bubbles rising in infinite liquids. *Transactions of the Institution of Chemical Engineering*, 51:116–120, 1973.

[35] R. Clift, J. R. Grace, and M. E. Weber. *Bubbles, drops, and particles*. Academic Press, New York, 1978.

[36] M. van Sint Annaland, N. G. Deen, and J. A. M. Kuipers. Numerical simulation of gas bubbles behaviour using a three-dimensional volume of fluid method. *Chemical Engineering Science*, 60(11):2999–3011, 2005.

[37] V. Ahuja, A. Hosangadi, S. Mattick, C. P. Lee, R. E. Field, and H. Ryan. Computational Analyses of Pressurization in Cryogenic Tanks. In *44th AIAA/ASME/SAE/ASEE Joint Propulsion Conference & Exhibit*, pages 1–12, July 2008.

[38] C. L. Merkle, J. Z. Feng, and P. E. O. Buelow. Computational modeling of the dynamics of sheet cavitation. In *3rd International Symposium on Cavitation*, Grenoble, France, 1998.

[39] F. R. Menter, M. Kuntz, and R. Langtry. Ten Years of Industrial Experience with the SST Turbulence Model. *Turbulence Heat and Mass Transfer 4*, 4:625–632, 2003.